An Atomic Magnetometer based on Nonlinear Magneto-Optical Polarization Rotation

A thesis submitted in partial fulfillment of the requirement
for the degree of Bachelor of Science with Honors in
Physics from the College of William and Mary in Virginia,

by

Jiahui Li

Accepted for Honors

Advisor: Prof. Irina Novikova

Prof. David S. Armstrong

Prof. Paul Davies

Williamsburg, Virginia
May 19 2022

Contents

Acknowledgments

I would like to pay my special regards to my advisor Professor Irina Novikova for her tireless mentoring. This project would not have been possible without her. I'd like to express my deepest thanks to the AMO group at William & Mary, especially Savannah and Charris who helped me with their expertise in doing a lot of research and I came to know about so many new things.

I would like to thank William & Mary for providing such a precious opportunity. I am very grateful to my family and friends who always supported me during college.

List of Figures

Abstract

Magnetometers with high precision and accuracy have wide applications across various areas. We are developing an atomic magnetometer based on nonlinear magneto-optical rotation (NMOR). The magnetometer measures the polarization rotation of a light field, which is proportional to the magnetic field strength. However, such a magnetometer usually has a limited operation range and stops working for fields stronger than the Earth's magnetic field. To overcome this shortage, we implement frequency and amplitude modulation that induces side frequencies in the Fourier space which allows us to measure strong magnetic fields, up to 200 mG. We have achieved 60 pT sensitivity for the zero resonance using a quarter-waveplate and compensation coils. We further optimize the sensitivity of the side resonance to the nT level by separating the probe and pump beam. We finally generate a squeezed pump beam using polarization self-rotation and observe a noise reduction below the shot-noise-limit, which leads to a factor of two improvement on the SNR.

Chapter 1

Introduction

As any charged or magnetic object is affected by a magnetic field, magnetometers have wide applications across many areas. In geophysics, they are commonly used to map a large range of geologic maps by detecting the differences in the earth's magnetic field caused by the differing nature of rocks. Alternatively, in medical treatment, magnetometers offer attractive non-invasive diagnostics to ECG or electroencephalographs. They can also be used to detect submarines or unexploded landmines for military purposes. Most importantly, high precision magnetometer could be used in metrology to test scientific theories.

There are two types of magnetometers: vector magnetometers that measure the vector components of a magnetic field and scalar magnetometers that measure only the magnitude of the magnetic field. Each type can be further divided into subcategories, and the optical Faraday rotation magnetometer, in which the strength of the magnetic field results in the rotation of the light polarization, is one of the scalar magnetometers. It can have sensitivity as high as femto Tesla (10^{-15}T) level while typical magnetometers of other types have sensitivity ranges from sub-fT to pT. One unique advantage of the Faraday rotation magnetometer is that we are able to image a spatially-inhomogeneous magnetic field by recording the spatial change of the polarization. This is particularly useful in the quantum tracker project where we want

to trace the trajectories of electrons or other charged particles after they scatter.

An optical Faraday rotation magnetometer has already been built with great precision at 10 fT sensitivity level [1]. However, such a magnetometer has a poor range of operation in that it only measures extremely small magnetic fields about nT around zero. For many practical usages of the magnetometer such as the particle detector, we will need a larger operation range, up to the 10 μT level, while still keeping sufficiently high sensitivity.

Previously, we developed an atomic magnetometer based on nonlinear magneto-optical rotation (NMOR) in my junior research. We used an amplitude modulated laser interacting with a ^{87}Rb vapor inside a glass cell at room temperature that induces side resonances at strong magnetic fields [2]. We achieved an operation range at the 10μT level with 0.5nT sensitivity.

We divide our experiments into two parts. In the first part, we further improve the performance of the magnetometer until it is limited by the shot-noise. We use a frequency-modulated laser since our detection system is very sensitive to amplitude change. We also separate the probe and pump beam to eliminate the residual signal caused by the spurious amplitude modulation. We confirm that our signal is indeed shot-noise-limited (SNL) by analyzing the noise composition. In the second part, we implement a squeezed state of light to the probe beam which allows us to surpass the noise level below the shot noise.

This paper is structured as follows. We discuss the theoretical background for the Faraday rotation, the core physics phenomenon we used to measure the magnetic field, in section II. In sections III and IV, we present the setup and results using a frequency-modulated laser and two beams respectively. We confirm that our signal is optimized to the SNL regime by these classical techniques. In section V, we introduce the quantum electrodynamics (QED) and particularly the squeezed state of light. In

section VI, we implement a squeezed probe beam and show the noise reduction below the shot noise. Finally, in section VII, we conclude the experiment and discuss future work that could be done in this direction.

Chapter 2

Faraday Rotation

Faraday rotation is a physical phenomenon in which a linearly polarized light is sent through a medium and consequently the polarization of the light rotates at an angle that is proportional to the magnetic field strength applied to that medium. Hence, by measuring the rotation angle, we could calculate the magnetic field (Fig 2.1).

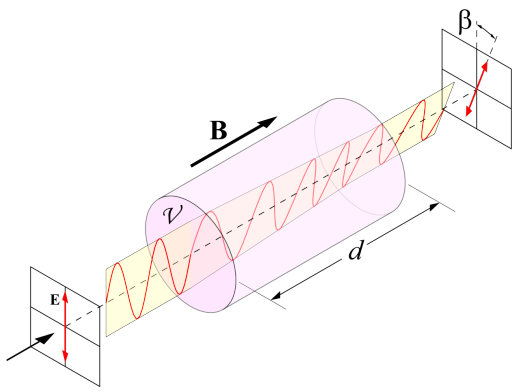

Figure 2.1: The incident light is linearly polarized. Its polarization is rotated by angle β after passing through a Rb vapor cell. d is the length of the medium and ν is the Verdant constant of the medium.

In this section, we will give a full description of the Zeeman effect, electromagnetically induced transparency, and eventually the Faraday effect.

2.1 Zeeman Effect

The Zeeman effect is the effect of splitting degenerate energy levels of atoms in the presence of a magnetic field. The Hamiltonian H of atoms in the presence of an

external magnetic field B_{ext} is

$$\hat{H} = \hat{H}_0 + \hat{H}_z \tag{2.1}$$

where $\hat{H}_0$ is the unperturbed atomic Hamiltonian and

$$\hat{H}_z = -\vec{\mu} \cdot \vec{B}_{ext}. \tag{2.2}$$

$\vec{\mu}$ is the magnetic moment of the atom, which can be obtained by

$$\vec{\mu} = -\frac{\mu_B(g_l\vec{L} + g_s\vec{S})}{\hbar} \tag{2.3}$$

with μ_B being the Bohr magneton. $\vec{L}$ and $\vec{S}$ are the orbital and spin angular momentum with g_l, g_s their respectively gyromagnetic ratios.

If we have a relatively weak external magnetic field B_{ext} and the spin-orbit interaction dominates over the effect of B_{ext}, we could treat H_z as a perturbing Hamiltonian. Using perturbation theory, one may find that the Zeeman correction to the energy E_z is

$$E_z = \langle nljm_j|H_z|nljm_j\rangle = \mu_B g_j B_{ext} m_j \tag{2.4}$$

where g_j is the Landé g-factor and n, l, j, m_j label quantum numbers for energy level, angular momentum, total angular momentum, and projection of total angular momentum [3]. Hence, we can see that the degenerate energy levels of different m_j split by an amount proportional to the external magnetic field B_{ext}.

2.2 Light Polarization

For now, we use a classical plane wave to approximate our laser. Suppose the wave traverses in the $\hat{z}$ direction, then planar traveling wave solutions of the Maxwell's equations are given by

$$\vec{E}(z,t) = E_x e^{ikz-iwt}\hat{x} + E_y e^{ikz-iwt}\hat{y} \tag{2.5}$$

where E_x, E_y are complex scalars that specify components of the electric field $\vec{E}$ in $\hat{x}, \hat{y}$ directions.

The polarization indicates the direction of the oscillation of $\vec{E}(z,t)$. A linear polarization means that the $\vec{E}(z,t)$ only oscillates in one direction, that is, either E_x or E_y is zero. Meanwhile, a circular polarization means that the electric field is continuously changing between $\hat{x}$ and $\hat{y}$ (Fig 2.2). For any linearly polarized light, we can decompose it into one clockwise and one counter-clockwise circular component.

Now, there are two requirements for light to excite an electron from one state to another. First, the frequency of the light must match or be close to the energy difference between these two states, known as the Rabi frequency Ω. We use detuning Δ to represent the frequency difference between the light and Ω. Second, the transition dipole moment of these two states determines the required polarization of the light. Usually, the transitions from $m_j = \pm 1$ ground state to the excited state need circularly polarized light. If these two circular components $\sigma_\pm$ match the energy difference between the excited state and two ground states, that is, the detuning $\Delta = 0$, we can represent this using a simplified three-level system (Fig 2.3).

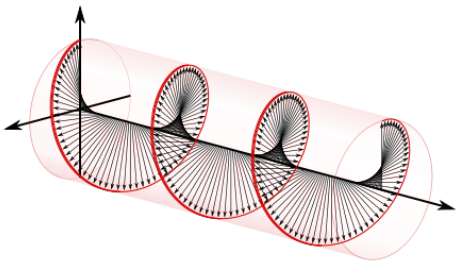

Figure 2.2: A counterclockwise circularly polarized light is viewed from the receiver.

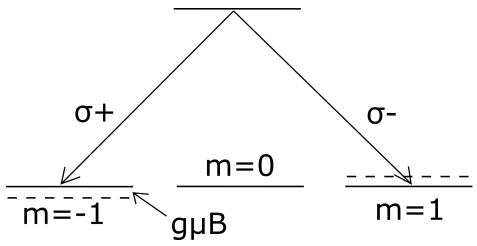

Figure 2.3: Solid lines represent the degenerate energy level without magnetic field and dashed states means split energy level caused by Zeeman effect. $\sigma_\pm$ corresponds to left and right circularly polarized light components.

Polarization Detection

Since a change of polarization does not affect the intensity of the light, we cannot simply use a photodiode to detect the polarization of light. A common approach to polarization detection requires a polarizing beam splitter (PBS) which separates the light into vertical and horizontal polarized components. Measuring the intensity of individual components and the difference between them gives us the polarization rotation angle.

2.3 Electromagnetically Induced Transparency

We combine our laser and atoms in this subsection. We consider the same three-level system as an approximation of our atoms. We send a linearly polarized light through the atomic vapor and its two circular components are resonant with two atomic absorptions. Naively, one may think that majority of the light would be absorbed as both of them are close to the energy difference. However, with this specific three-level ladder configuration, there is a solution named a "dark state" where an atom cannot absorb or emit photons, so this atomic vapor becomes transparent to the laser; this is known as electromagnetically induced transparency (EIT).

While the EIT changes atomic absorption corresponding to the imaginary part of the electric susceptibility χ, we are more interested in the change of the refractive index, the real part of χ. We now use a density matrix to find out the change in the susceptibility χ. Label $m_j = \pm 1$ states as states 1,2, $\sigma_{\mp}$ as electric field 1,2 and the excited state as state 3. The density matrix of a three level system is given by

$$\rho = \begin{bmatrix} \rho_{11} & \rho_{12} & \rho_{13} \\ \rho_{21} & \rho_{22} & \rho_{23} \\ \rho_{31} & \rho_{32} & \rho_{33} \end{bmatrix}. \tag{2.6}$$

Using the slow rotation wave approximation, the Hamiltonian of the three-level sys-

tem can be written as

$$H_{RWA} = \begin{bmatrix} -\hbar\Delta_1 & 0 & -\hbar\Omega_1^* \\ 0 & -\hbar\Delta_2 & -\hbar\Omega_2^* \\ -\hbar\Omega_1 & -\hbar\Omega_2 & 0 \end{bmatrix} \tag{2.7}$$

where Δ_i represent the detuning between the electric field i and the state i, and Ω_i is the Rabi frequency for field i. In our specific scenario, two incident fields are two circular components of a linearly polarized field, that is, $|\Omega_1| = |\Omega_2| = |\Omega|$. If both detuning $\Delta_1 = \Delta_2 = 0$, we have an eigenstate of the Hamiltonian, the dark state, given by

$$|D\rangle = \frac{1}{\sqrt{|\Omega_1|^2 + |\Omega_2|^2}}(\Omega_2|1\rangle - \Omega_1|2\rangle) \tag{2.8}$$

and we know the probability density $\rho_{11} = \rho_{22} = \frac{1}{2}$ in this case.

Notice that for our atomic magnetometer, we have a magnetic field B that evenly splits $m_j = \pm 1$ degenerate states, then we get $\Delta_{1,2} = \pm\mu g_j B$ and $\delta = \Delta_1 - \Delta_2 = 2\mu g_j B$ (Sec. 2.1). Since we are only interested in the linear susceptibility χ of two incident fields, which is related to ρ_{31}, ρ_{32}, we may assume that $\rho_{11} = \rho_{22} = \frac{1}{2}$ in the steady state solution for simplification. Applying the Maxwell-Bloch equations

$$i\hbar\frac{\partial\rho}{\partial t} = [H, \rho] + \frac{1}{2}\{\Gamma, \rho\} \tag{2.9}$$

where ρ is the density matrix and we artificially add terms related to decoherence Γ instead of commuting the anti-commutator. In the steady state solution, we find ρ_{31} and ρ_{32} as

$$\rho_{31} = \frac{i\Omega_1}{\gamma}\left[\frac{1}{2} - \frac{|\Omega|^2}{\gamma(\gamma' - i\delta) + 2|\Omega|^2}\right], \tag{2.10}$$

$$\rho_{32} = \frac{i\Omega_2}{\gamma}\left[\frac{1}{2} - \frac{|\Omega|^2}{\gamma(\gamma' + i\delta) + 2|\Omega|^2}\right]. \tag{2.11}$$

where γ, γ' are decay of the excited state and collisional decoherence between two ground states respectively. This gives us the susceptibility

$$\chi_1 = \frac{P_{13}^2}{\hbar\epsilon_0}\frac{\rho_{31}}{\Omega_1} \quad \text{and} \quad \chi_2 = \frac{P_{23}^2}{\hbar\epsilon_0}\frac{\rho_{32}}{\Omega_2} \tag{2.12}$$

where P_{ab} is the transition dipole moment and ϵ_0 is the vacuum permittivity [4]. The refractive indices are related by $n = 1 + Re(\chi)/2$, so we find

$$n_1 = 1 + \frac{P_{13}^2}{4\epsilon_0\hbar\gamma}\frac{\delta \cdot 2|\Omega|^2/\gamma}{(\gamma' + 2|\Omega|^2/\gamma)^2 + \delta^2}, \tag{2.13}$$

$$n_2 = 1 - \frac{P_{23}^2}{4\epsilon_0\hbar\gamma}\frac{\delta \cdot 2|\Omega|^2/\gamma}{(\gamma' + 2|\Omega|^2/\gamma)^2 + \delta^2}. \tag{2.14}$$

Hence, we see that the two fields have the opposite change in the refractive indices (Fig. 2.4).

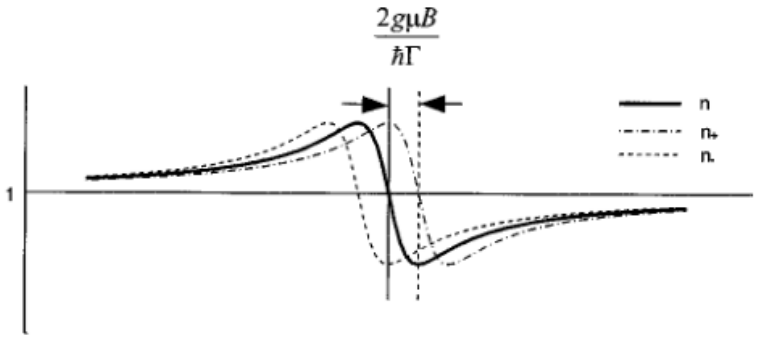

Figure 2.4: The x-axis is the detuning δ and the y-axis is the refractive indexes n.

Since two circular components of the laser traverse the atomic vapor with different velocities, when we combine them at the exit into a linearly polarized laser, the polarization rotates at an angle β that is given by

$$\beta = \pi(n_1 - n_2)\frac{d}{\lambda} \tag{2.15}$$

where λ is the wavelength of the light. This is exactly the Faraday rotation and by measuring the rotation angle β, we are able to measure the magnetic field strength. However, if the Zeeman splitting becomes too large in a very strong magnetic field, the laser frequencies are no longer in a two-photon resonance with the corresponding atomic levels, and the approximations we made in the calculations are no longer valid. The refractive indices would not be magnetic-field dependent for a strong magnetic field, which limits our range of operation.

2.4 Amplitude Modulation and Frequency Modulation

In order to increase the narrow operation range, we use amplitude modulation (AM) which induces frequency sidebands and side resonances. AM continuously changes the amplitude of our signal with modulation frequency f_m (Fig. 2.5). Suppose the original signal, the carrier $c(t) = A_c \sin(2\pi f_c t)$, is a sine wave and the modulation signal, the messenger $m(t) = A_m \cos(2\pi f_m t + \phi)$, is a cosine wave, the modulated signal $y(t)$ is given by

$$y(t) = \left[1 + \frac{m(t)}{A_c}\right] c(t). \tag{2.16}$$

Using trigonometry identities, one may simplify Eq. 2.16 to a sum of three sine waves as

$$y(t) = c(t) + \frac{1}{2} A_m \{\sin[2\pi(f_c + f_m) + \phi] + \sin[2\pi(f_c - f_m) - \phi]\} \tag{2.17}$$

where the latter two terms are sidebands of the modulated signal (Fig. 2.6). Hence, for an amplitude modulated laser, we get an AM signal with side-bands f_m away from its original frequency ω_0.

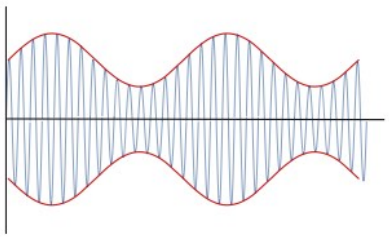

Figure 2.5: The red signal is a sine carrier signal with frequency f_c and amplitude A_c while the blue signal is the modulated signal with original frequency f_m.

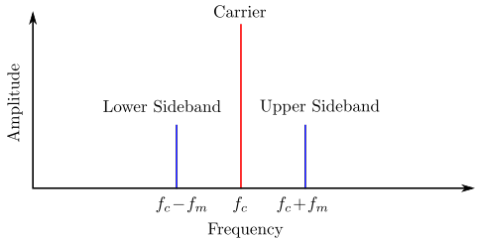

Figure 2.6: Two side frequencies of $f_c - f_m$ and $f_c + f_m$ emerge as the result of the amplitude modulation.

Another modulation technique we used is the frequency modulation (FM) which

induces frequency sidebands and side resonances similar to AM. For a sinusoidal modulating signal $f_m(t) = A_m \cos(w_m t)$ with amplitude A_m and modulation frequency w_m, the phase angle θ of the FM signal is given by

$$\theta = \omega_0 t + h \sin(\omega_m t) \tag{2.18}$$

where ω_0 is the original frequency and h is the modulation index. We can expand the FM signal $y(t)$ into its Fourier series, that is,

$$y(t) = Re(Ae^{i\omega_0 t} e^{ih \sin \omega_m t}) \tag{2.19}$$

$$= Re(Ae^{i\omega_0 t} \sum_{n=-\infty}^{\infty} J_n(h) e^{in\omega_m t}) \tag{2.20}$$

$$= A \sum_{n=-\infty}^{\infty} J_n(h) \cos(\omega_0 + n\omega_m)t \tag{2.21}$$

for some amplitude A while $J_n(h)$ is the Bessel function of the first kind of order n. We can see that the FM signal has side-bands $n\omega_m$ away from its original frequency ω_0. We will only consider the $n = 1$ side-bands here, as side-bands with higher n have much smaller amplitude.

Consider the simplified three-level system in the previous subsection with a modulated signal. While we have the Zeeman shift caused by an external magnetic field, we also have side-bands induced by the AM or FM (Fig. 2.7). If these side-bands of our laser come near to shifted energy levels, we have the exact condition for EIT as discussed above. Again, we have the Faraday rotation which is proportional to the external magnetic field since the detuning of the incident field is small in this case. Therefore, by measuring the modulation frequency for which side resonances occur, we could calculate the unknown magnetic field much larger than zero.

Although AM and FM seem to both yield side resonances that allow us to measure strong magnetic fields, they have subtle differences when implemented in our

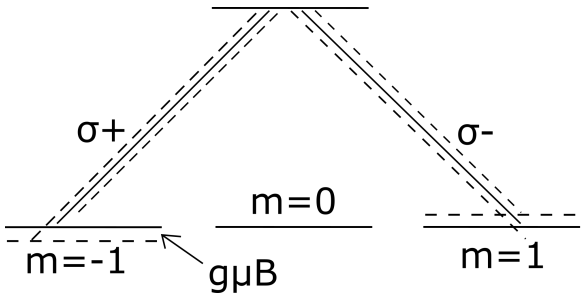

Figure 2.7: The original frequency of the light is shown in solid lines and sidebands are shown with dashed lines. These side-bands, generated by the AM or FM, prompt Faraday rotation as well, resulting in side peaks in the signal.

experiments [2]. Since we rely on the intensity measurement of the vertical and horizontal polarized component of light to find its polarization rotation angle, we are extremely susceptible to the intensity fluctuation and the constant intensity change brought by AM. On the other hand, an internally frequency-modulated light has a spurious amplitude modulation because the laser cavity has different gains for different frequencies. Hence, each modulation technique has its limitation, and we will discuss how to overcome these problems in later sections.

Chapter 3

Single Coherent Beam

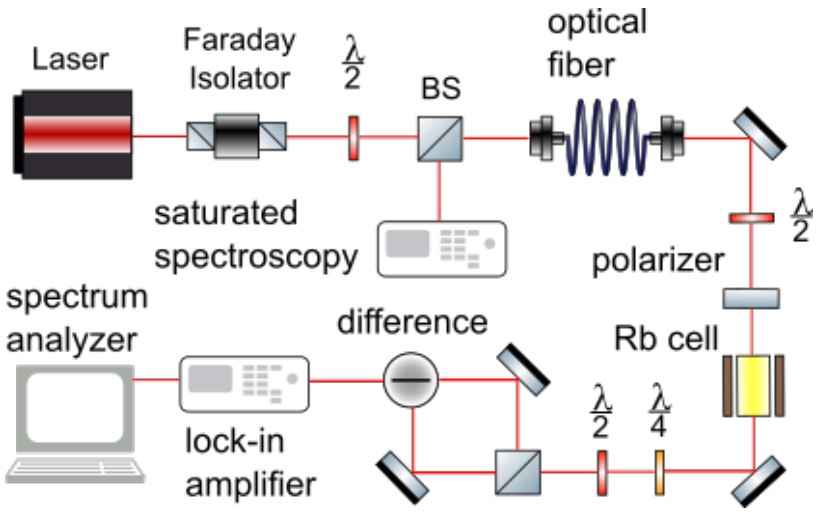

Figure 3.1: The laser is internally frequency modulated in this one beam setup.

The first experiment we conduct only uses one coherent laser beam. A schematic of the apparatus is presented below in Fig. 3.1. We use a frequency-modulated diode laser as our light source. We first pass it through a Faraday isolator that prevents any reflected light. The laser beam is then split into two parts and a half-waveplate is used to control the splitting ratio.

The first part of the laser beam is sent into a spectroscope and an interferometer to monitor the status of our laser. The saturated spectroscopy precisely marks the

absorption frequency of ^{87}Rb atoms, the medium of the diode laser. It is especially helpful if we need to lock the frequency of the laser to transition frequencies or near them while it could also indicate whether we have a mode jump in the medium of the laser. Next, we use a Fabry–Pérot interferometer to determine the mode of the laser. Ideally, we want the laser to have only one mode corresponding to the evenly spaced sharp signal of the interferometer. After we implement the FM, they become evenly spaced wiggling signals and we maximize the height to optimize the performance of the laser. A graph of signals of the saturated spectroscopy and the Fabry–Pérot interferometer is shown in Fig. 3.2.

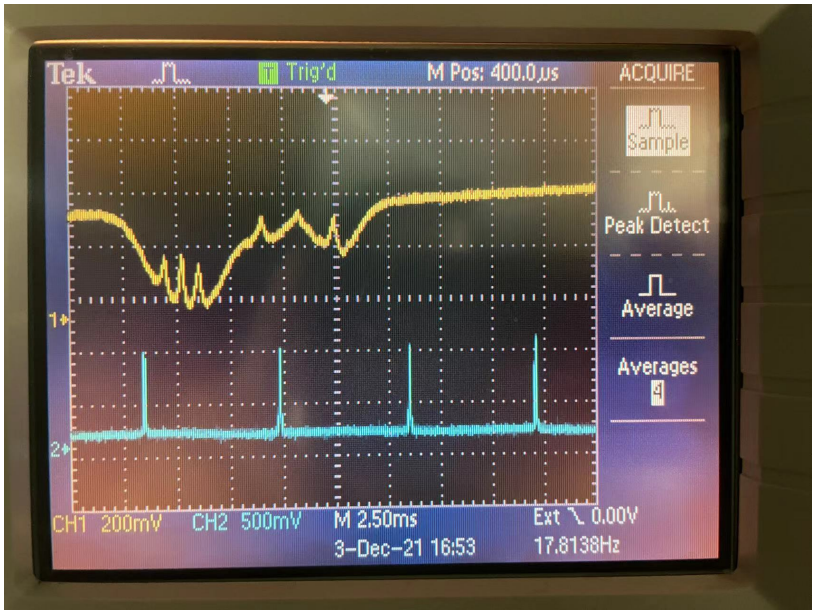

Figure 3.2: Typical signals of the saturated spectroscopy (yellow line) and the Fabry–Pérot interferometer (blue line). The right three yellow peaks represent $F = 2 \rightarrow F' = 2$, cross-over, and $F = 2 \rightarrow F' = 1$ transitions of ^{87}Rb. Blue peaks are evenly spaced as references.

We pass the second part of the laser through a single-mode optical fiber that puts constraints on the spatial mode of the laser. Then we control the power using a have-waveplate and a linear polarizer. We use a beam expander that increases the size of the laser to maximize interaction between the laser and vapor atoms and the

rotation angle response. After adjusting the power and beam size, the laser passes through a ^{87}Rb vapor cell with magnetic shielding. We investigate both $F = 2$ to $F' = 1$, $F' = 2$ transitions of ^{87}Rb. We find that the $2 \to 1$ transition has a stronger response and better sensitivity than the $2 \to 2$ transitions. Inside the shielding, we use a Helmholtz coil to simulate a uniform parallel magnetic field and a heater to increase the vapor density. Furthermore, there are two sets of compensation coils to reduce the small inhomogeneous part of the magnetic field.

For the laser light emerging from the cell, we use a quarter-waveplate to balance the offset in our signal caused by the spurious AM. This offset might also come from the residual circular component of the polarization caused by polarization self rotation. We rotate the linear polarization using a half-waveplate to calibrate the zero of the magnetometer so that there is no polarization rotation for a zero magnetic field. Finally, we use a beam splitter whose splitting ratio depends on the polarization, and measure the signal difference between the two channels of the beam splitter. The difference signal is proportional to the polarization rotation angle and therefore to the magnetic field strength.

Since we modulated the laser, we use both a lock-in amplifier and a spectrum analyzer to analyze the strength of the response and the sensitivity. Using a lock-in amplifier, we are able to observe side resonance peaks that allow us to measure the magnetic field away from zero (Fig. 3.3) which agrees with our theory in the previous section. Since the position of the side resonance is proportional to the modulation frequency, we can shift this peak to an arbitrary position and use it to get highly sensitive magnetic field measurements.

Next, we present the problem with this setup and the corresponding improvement we made to solve it.

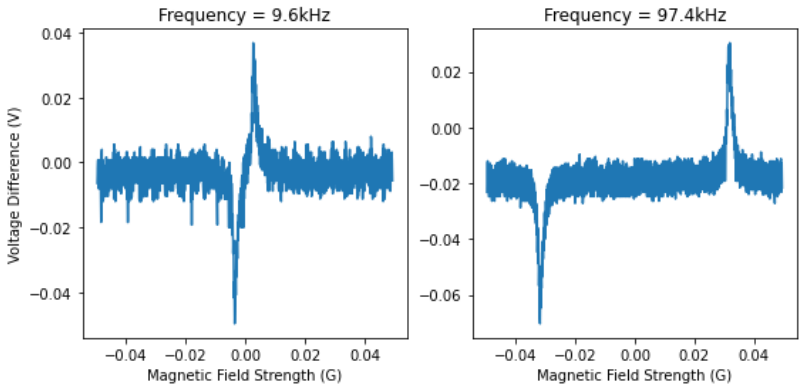

Figure 3.3: We sweep the parallel B field for different modulation frequencies in a shielded environment. The out-of-phase component of the signal is presented. The positions of the side peaks are proportional to the modulation frequencies.

3.1 Compensation Coils

To measure a strong magnetic field away from zero, the side resonances are essential and determine the sensitivity of our measurements. However, we find that the side resonances have significantly worse sensitivity than the zero resonance, which is not predicted by our model. This low performance of side resonances partly results from the inhomogeneity of the magnetic field. While the Helmholtz coil only produces a highly homogeneous magnetic field near its center, the vapor cell has a certain length so its tail experiences a magnetic field gradient that detriments our sensitivity. For a weak magnetic field that induces the zero resonance, the gradient is small and we don't observe this effect. However, as side resonances require a strong magnetic field, we suffer from this magnetic field gradient.

We use two compensation coils on both sides of our vapor cell to reduce this effect. To achieve the best compensation, we use a voltage divider to keep a constant ratio between the current of the main coils and side coils (Fig. 3.4). The optimal ration is determined based on the strength of side resonances. We see a significant improvement in side resonances after we implement compensation coils.

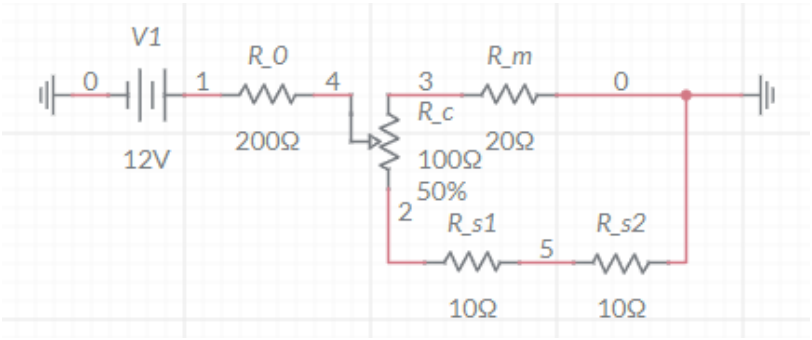

Figure 3.4: The schematics for the voltage divider. We use R_c to control the splitting ratio. R_m is the main coil and R_{s1}, R_{s2} are side coils. Resistances values are approximated and not exact.

3.2 Calibration

We use both a lock-in amplifier and a spectrum analyzer to process our data. When we sweep the external magnetic field, only the lock-in amplifier recovers the modulated signal. On the other hand, we use the spectrum analyzer to calculate the sensitivity for a DC magnetic field as it yields more precise measurements.

Since we control the Helmholtz coil using a function generator, we have to first calibrate the scale between the voltage of the function generator and the magnetic field strength. We use the lock-in amplifier to find the peak position for a sweeping magnetic field. From the Zeeman effect, we calculated that 0.7 mG of the magnetic field corresponds to 1 kHz of the modulation frequency. We can also find the particular voltage associated with each peak using the recorded time. Eventually, we use linear regression to find the conversion between magnetic field $B(mG)$ and voltage $V(V)$, and it is given by

$$B = 280.7V - 21.4 \tag{3.1}$$

with the fitting score R^2 of 0.99999. We see a strong linear relationship between B and V as we use the Helmholtz coil to generate the magnetic field. Notice there is a small negative intercept indicating that we may need a threshold voltage to generate

side peaks. Hence, for a small magnetic field near the zero resonance, we should ignore the intercept and only use the slope to calculate the magnetic field.

3.3 Sensitivity

We estimate the sensitivity using a spectrum analyzer with a DC magnetic field as it yields the best precision. We fine-tune the quarter-waveplate and the half-waveplate such that we have a minimal high-frequency response when there is no magnetic field. Then we calculate the signal to noise ratio (SNR) as

$$SNR = \frac{(\psi_s - \psi_0)^2}{\psi_n^2} RBW \tag{3.2}$$

where RBW is the resolution bandwidth of the spectrum analyzer and ψ_s, ψ_0, ψ_n are responses for the signal, offset, and noise respective [5]. The sensitivity is given by

$$S = \frac{\delta B}{SNR} \tag{3.3}$$

where δB is the magnetic field producing the signal.

For the zero resonance, we get $\psi_s = -74$ dBm, $\psi_0 = -98$ dBm, and $\psi_n = -108$ dBm for a small magnetic field $\delta B = 0.2807$ mG and the power of the laser is 3 mW. The corresponding sensitivity is $S = 59.78$ pT. Therefore, using only quarter-waveplate and compensation coils, we have already significantly improved the sensitivity from previous sub-nT level for a laser with 0.2 mW power to now the pT level for a laser with 3 mW power.

Our next step is to investigate the sensitivity of side resonances, which are expected to have a similar order of magnitude as the zero resonance. Furthermore, the use of a quarter-waveplate to balance the offset in our signal is only a contemporary solution that does not fix the source of this offset directly and the modulated beam still cannot be balanced perfectly. We now aim to develop a two-beam configuration to sidestep this problem before the implementation of a squeezed state of lights.

Chapter 4

Two Coherent Beam

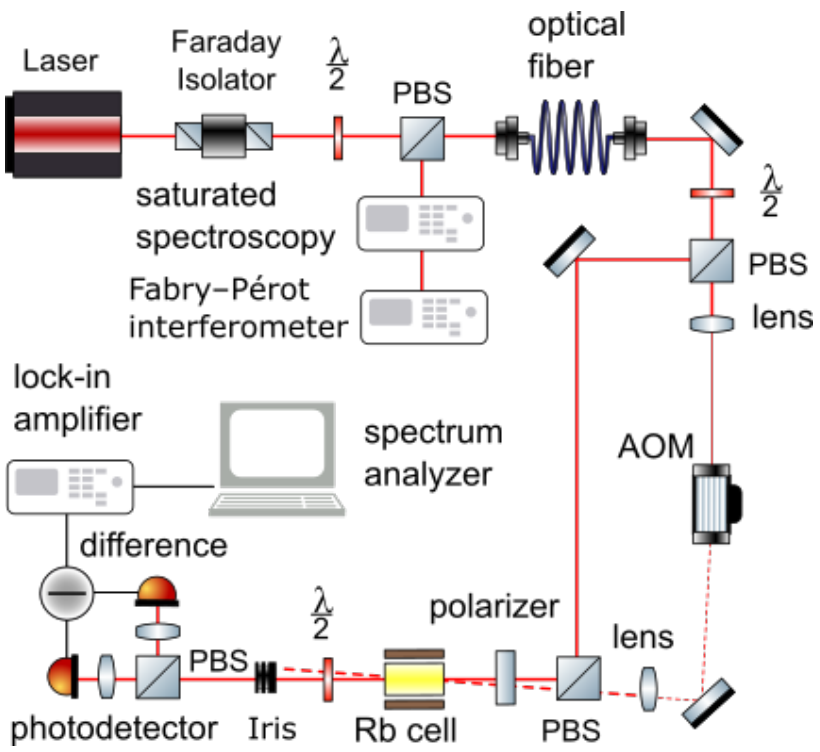

Figure 4.1: The laser is not internally frequency modulated. A dashed line represents an amplitude modulated laser while a solid line means unmodulated light.

In this improved experiment, we split the laser into two beams and send them both through the Rb cell (Fig. 4.1). Our laser, in this case, is not internally frequency modulated and is still a coherent light source. We keep all laser monitor

components, i.e. saturated spectroscopy and Fabry-Perot interferometer, the same as in the previous experiment.

The first change, compared to the single coherent configuration, is the PBS after the optical fiber. One of the split beams, called the probe beam, is not modulated. It passes through the Rb cell while its polarization rotates because of the Faraday rotation. Then we measure the rotation angle using another PBS and two photodiodes as discussed before. We use two additional lens to focus the probe beam such that it is completely captured by the photodiodes. Finally, we can calculate the magnetic field from the rotation angle. Notice that since the probe beam is not modulated, it does not have any high frequency offset in the lock-in signal. Hence, we sidestep the offset problem and use another split beam to induce side resonances.

The second beam, named the pump beam, is first focused after the PBS and then amplitude modulated by an acousto-optic modulator (AOM). An oscillating electric signal drives sound waves in the AOM, which are effectively periodic expansion and compression planes which therefore changes the refractive index, so parts of the incident light diffract with a modulated amplitude. The pump beam also passes through the Rb cell but with an angle to the probe beam such that it is blocked by an iris before the detection. While we do not directly observe the pump beam as it will cause an offset in the lock-in signal, the pump beam prepares these Rb atoms into the dark state. Since the pump beam is amplitude modulated, it could interact with energy levels shifted by the Zeeman effect and changes the refractive indexes for two circular components of the probe beam as well. As the result, although the probe beam by itself cannot see Zeeman shifted energy levels, its polarization still rotates when the induced frequencies of the pump beam coincide with transition energies of shifted energy levels.

We take a few steps to check the alignment of two beams. When we block the

probe beam, we see no lock-in signal meaning that the pump beam is properly blocked by the iris. If we block the pump beam, we get zero signal as expected since the probe beam is not modulated. Lastly, we check that the signal is zero for a zero magnetic field indicating that we have no offset.

The data processing is done similarly to the single beam configuration using a lock-in amplifier and a spectrum analyzer.

4.1 Noise Composition Analysis

As we aim to implement squeezing to our probe beam that would increase our sensitivity only if our signal is SNL, we conduct a noise composition analysis. The noise N consists of two terms, the electronic noise and the shot noise, given by

$$N = A + B \cdot P \tag{4.1}$$

where B is a factor affected by lock-in amplifier gain, and P is the laser power, A is the electronic noise or the dark noise, and $B \cdot P$ is the shot noise which scales with the laser power.

Ideally, A is constant noise from photodiodes and the spectrum analyzer. However, when we amplify the optical signal using the lock-in amplifier, we are also amplifying its electronic noise while the lock-in amplifier may have different electronic noises for different gains. Hence, we first characterize the electronic noise for all gains of the lock-in amplifier. We block the laser and record the constant signal for each gain using an oscilloscope to get its Fourier spectrum (Fig. 4.2). We find that the lock-in amplifier has small electronic noise for $V = 30$ mV, and 1 mV as these noise levels do not scale up with the gain. As $V = 1$ mV saturates the lock-in amplifier quickly for a small laser signal, we further investigate the noise composition for $V = 30$ mV and 10 mV gains.

To determine whether the electronic noise or the shot noise dominates our signal, we look at the SNR. If our signal is limited by constant electronic noise, we can always amplify it to get a better SNR. Hence, we increase the gain and measure how the SNR scales with it. If the SNR is unchanged while we increase the lock-in amplifier gain, we may conclude it is in the SNL regime. Again, we Fourier transform our signals while the laser is unblocked. We find that our signal is SNL with $V = 30$ mV and 10mV gains which also returns the best SNR (Fig. 4.3).

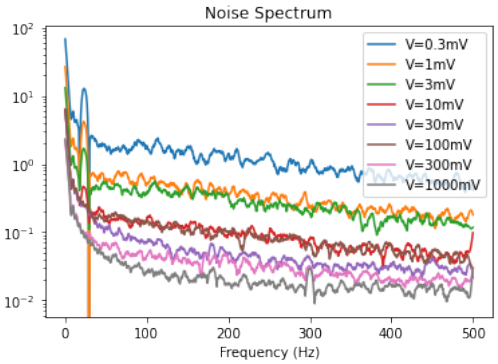

Figure 4.2: The gain of the lock-in amplifier is reciprocal of the voltage.

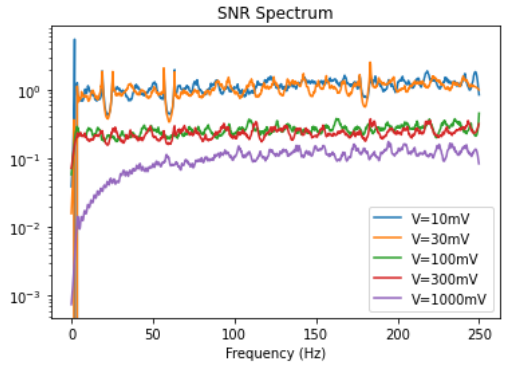

Figure 4.3: Larger gains than V=10mV necessarily saturate our signal so they are not measured.

4.2 Laser Power Optimization

This two beam setup introduces a few more parameters such as the pump power and the light intersection angle than the previous experiment to optimize, so we need to optimize the SNR of our signal in hyper-dimensional parameter space. We first focus on the powers of the probe and pump beams since these two parameters are easier to change and have major effects on our signal.

We set the modulation frequency to 400 kHz, corresponding to a side resonance around 500mG while locking the laser frequency at the $2 \rightarrow 1$ transition. The magnetic field sweeps around the side resonance and we conduct a grid search that varies

powers for both beams from 0.5 mW to 6 mW. We extrapolate a smooth curve from the noisy signal to estimate the response slope (Fig. 4.4). Since the total power of two beams has an upper limit of about 7 mW, the range of the pump power is limited by the probe power. Notice the actual pump power is double the measured value since the pump is amplitude modulated. We find that 1 mW probe power gives us the strongest response and the slope is positively related to the pump power.

Notice that we used a large step in the grid search as we need to cover a large parameter space, so we decided to investigate more closely around the optimal powers in the grid search. Also, instead of using the response slope as the metric, we perform a complete SNR analysis for this refined measurement since different powers may have different noise levels. In this case, we take two stationary magnetic fields on the side resonance whose difference is the signal. We get the noise using Fourier transformation again. We set the pump power to 1.6 mW and vary the probe power from 1.5 mW to 3 mW (Fig. 4.5). Although different probe powers have similar SNR, we find the best SNR occurs at 1.75 mW while we suspect the measurement for 2.75 mW probe power is an outlier and do not take it into consideration. We repeat the process for the pump beam whose power ranges from 1.4 mW to 3.4 mW with a constant 1.75 mW probe beam (Fig. 4.6). The SNR seems to increase with the probe power until it is limited by the laser output and we do not find a local extremum for the pump power, so higher pump power may give an even better SNR.

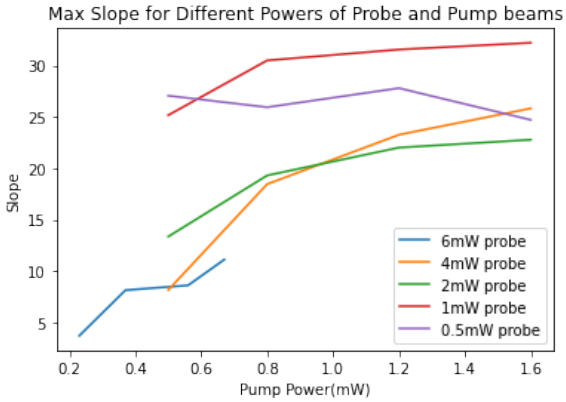

Figure 4.4: The slope is normalized and only used for comparison between different powers.

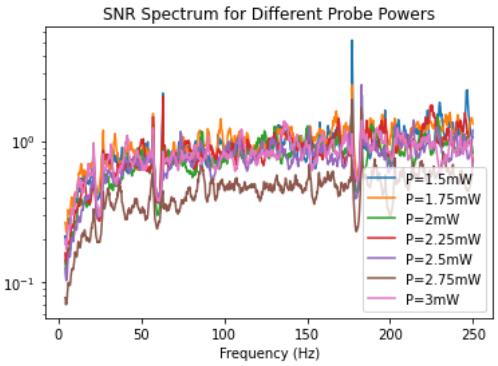

Figure 4.5: The SNR spectrum for probe power ranges from 1.5 mW to 3 mW in steps of 0.25 mW where the y-axis is unitless.

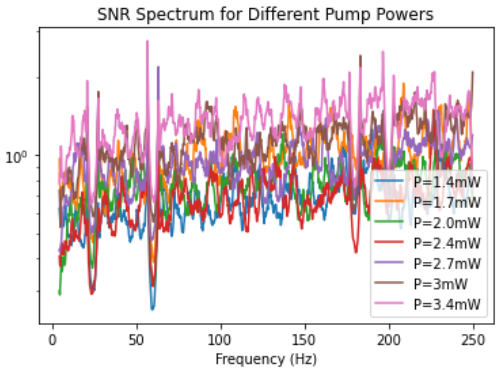

Figure 4.6: The SNR spectrum for pump power ranges from 1.4 mW to 3.4 mW where the y-axis is unitless.

4.3 Beam Configuration

After obtaining the optimal lock-in amplifier gain and laser beam powers, we investigate the effect of beam intersection angle on our signal. Although the obvious answer is that a smaller angle leads to a larger cross-area and a better SNR, it is still worth checking quantitatively the differences between our signals caused by different intersection angles because a larger intersection angle gives us a better spatial resolution on the magnetic field.

We use two mirrors after the optical fiber that reflects the pump beam to control the intersection angle. We record the separation distance between the probe and pump beam when they hit the iris before detection in order to measure the angle. We keep the modulation to be 400 kHz, the detuning at $2 \rightarrow 1$ transition, and the optimal powers found in the previous section. Since the laser power is held constant, we assume the noise level does not change, so we use a sweeping magnetic field and the signal response slope represents our sensitivity.

The probe beam size puts a minimal constraint on the size of the iris hole that it must be large enough for the probe to fully pass. Meanwhile, the iris needs to block

the pump beam otherwise the pump beam would leak into photodiodes. Hence, the lower limit of the distance between two beams at the iris is set by their sizes. On the other hand, the upper boundary of the intersection angle is set by the size of the holes of the Rb cell. We change the distance at the iris from 3 mm to 8 mm and record corresponding signals (Fig.4.7). For 3 mm separation at the iris, parts of the pump beam leak into photodiodes which detriment our sensitivity. While we find that a 4mm distance is about the minimum at which two beams are separated, the results confirm our hypothesis that a smaller separation distance yields better sensitivity. Nonetheless, the sensitivity of the largest separation of 8 mm is only about 10% worse than the optimal separation of 4.5 mm while the additional spatial information provided by a large angle might be worth the trade-off.

We further check the parallel beam configuration where the pump beam affects the probe beam only through the atom diffusion. Ideally, this should yield a better sensitivity than the intersection configuration [6]. To observe the improvement, however, we need to use a weak probe beam with power around 200 μW-300 μW. We keep all other parameters the same and measure the signal generated by a sweeping magnetic field. The distance between two parallel beams is limited by the size of the opening on the Rb cell as well as other physical constraints such as the size of the PBS. As the result, we only have one possible parallel configuration with a separation distance of 4 mm (Fig. 4.8). We find that although the parallel configuration loses the spatial resolution, it almost doubles the sensitivity and gives us the estimated nT level sensitivity at side resonances.

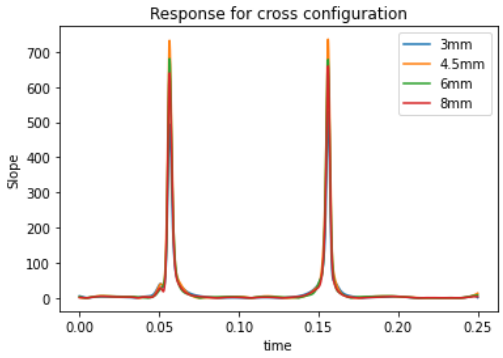

Figure 4.7: There are two periods shown in this graph.

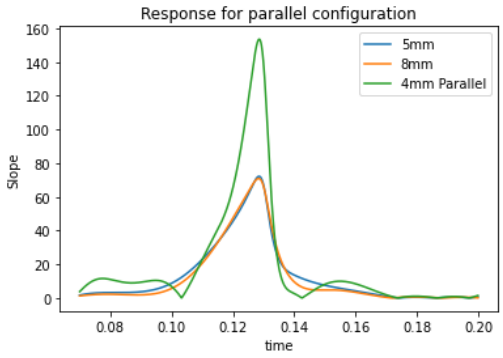

Figure 4.8: 5 mm and 8 mm separations represent intersected beams.

Chapter 5

Squeezed states of light

So far, we haven't considered the quantum nature of our laser yet. Using the classical description of the laser, we could model everything we need to make measurements. However, when we consider the sensitivity of our measurement, quantum mechanics imposes a fundamental limit on the classical laser, the shot-noise limit (SNL).

To describe SNL, we have to use quantum electrodynamics (QED) and quantize our laser field to an operator. While the spatial dependence is fully determined by boundary conditions, the temporal part of a plane electric field is given by

$$\hat{E}(t) = \sqrt{\frac{\hbar\omega}{\epsilon_0 V}}(\hat{a}e^{-i\omega t} + \hat{a}^\dagger e^{i\omega t}) \tag{5.1}$$

where V is the volume of the box, and $\hat{a}, \hat{a}^\dagger$ represent annihilation and creation operator of a photon respectively. We have the number operator $\hat{n} = \hat{a}^\dagger\hat{a}$ which satisfies $\hat{n}|n\rangle = n|n\rangle$. When we measure the electric field, we are measuring its power which is proportional to the square of the photon number n, so the sensitivity of our measurements is limited by the photon number statistical fluctuations $\Delta n = \sqrt{\langle\hat{n}^2\rangle - \langle\hat{n}\rangle^2}$.

The most classical state, the coherent state $|\alpha\rangle$, is an eigenstate of $\hat{a}$ such that

$$\hat{a}|\alpha\rangle = \alpha|\alpha\rangle. \tag{5.2}$$

One may find the photon number fluctuation Δn for the coherent state $|\alpha\rangle$ as

$$\Delta n = |\alpha| = \sqrt{\langle \hat{n} \rangle}, \tag{5.3}$$

known as the shot noise. The shot noise originates from the uncertainty principle for two quadrature operators $\hat{X_1} = \frac{1}{2}(\hat{a} + \hat{a}^\dagger)$, $\hat{X_2} = \frac{1}{2i}(\hat{a} - \hat{a}^\dagger)$ and

$$(\Delta X_1)^2 (\Delta X_2)^2 \geq \frac{1}{16}. \tag{5.4}$$

This means that we cannot precisely measure both the amplitude and the phase of an electric field simultaneously. For a coherent state, one could calculate that $\Delta X_1 = \Delta X_2 = \frac{1}{2}$. To surpass the SNL imposed by the uncertainty principle, we sacrifice the precision of one quadrature to allow a more precise measurement of another one.

We introduce the squeezing operator $\hat{S}(\xi) = exp[\frac{1}{2}(\xi \hat{a}^2 - \xi \hat{a}^{\dagger 2})]$ where $\xi = re^{i\theta}$ is the squeezing parameter. Using the Baker-Hausdorf lemma, we calculate the variance of quadrature operator for the squeezed state and coherent state. We find that

$$\frac{(\Delta X_{sqz})^2}{(\Delta X_{coh})^2} = e^{-2r}. \tag{5.5}$$

Notice that we do sacrifice the precision of the anti-squeezed quadrature to satisfy the uncertainty principle; a visualization of a comparison between a squeezed state and a coherent state is given in Fig. 5.1. Therefore, by measuring the squeezed quadrature, we can get a sensitivity lower than the SNL.

5.1 Balanced Homodyne Detection

In this section, we discuss the method to measure a squeezed state of light. As the squeezed state has less noise only in a particular quadrature, we cannot directly measure it using a photodiode. Rather, we use a technique named balanced homodyne detection that allows us to choose which quadrature to measure.

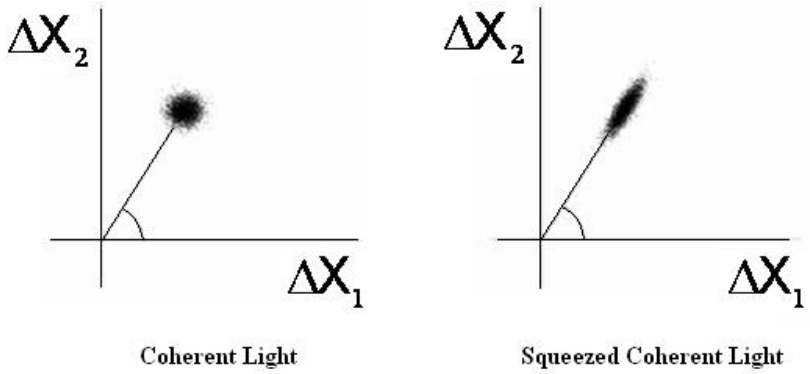

Figure 5.1: The uncertainty ball represents the noise when different quadratures of the signal are measured.

Shown in Fig. 5.2, we mix a strong coherent field in mode $\hat{b}$, named the local oscillator (LO), with the squeezed state of the light in mode $\hat{a}$ using a beam splitter (BS). Since the BS evenly splits two inputs beam, its outputs $\hat{c}$ and $\hat{d}$ are given by

$$\hat{c} = \frac{1}{\sqrt{2}}(\hat{a} + i\hat{b}), \qquad \hat{d} = \frac{1}{\sqrt{2}}(\hat{b} + i\hat{a}). \tag{5.6}$$

Then we use two photodiodes to measure the intensity of each beam. As the intensity is proportional to the number of photons, these measurements are simply $I_c = \langle \hat{c}^\dagger \hat{c} \rangle$ and $I_d = \langle \hat{d}^\dagger \hat{d} \rangle$. Eventually, we subtract signals from two photodiodes to cancel the coherent noise and the difference is given by

$$I_c - I_d = \hat{n}_{cd} = i\langle \hat{a}^\dagger \hat{b} - \hat{a}\hat{b}^\dagger \rangle. \tag{5.7}$$

Assuming the mode $\hat{b}$ is indeed in a coherent state $|\beta e^{-i\omega t}\rangle$ and the mode $\hat{a}$ has the same frequency ω, we can rewrite Eq. 5.7 as

$$\hat{n}_{cd} = 2|\beta|\langle \hat{X}(\theta) \rangle \tag{5.8}$$

where $\beta = |\beta|e^{-\psi}$, $\theta = \psi + \pi/2$, $\hat{a} = \hat{a_0} e^{-i\omega t}$, and

$$\hat{X}(\theta) = \frac{1}{2}(\hat{a_0} e^{-i\theta} + \hat{a_0}^\dagger e^{i\theta}) \tag{5.9}$$

is the quadrature operator at angle θ [7]. Notice that we could measure an arbitrary quadrature of the signal by changing the phase ψ of the LO. One may also check that by choosing a squeezed quadrature where $(\Delta\hat{X}(\theta))^2 < \frac{1}{4}$, we could have

$$(\Delta\hat{n}_{cd})^2 < |\beta|^2 \tag{5.10}$$

which surpass the coherent noise $|\beta|^2$.

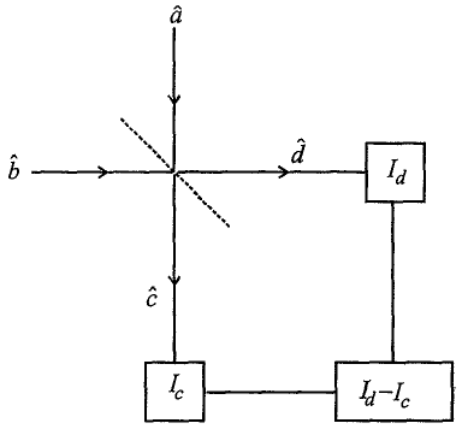

Figure 5.2: The dashed line represents a beam splitter and two intensities I_c, I_d represent two photodiodes. The subtracter is shown as $I_d - I_c$.

5.2 Polarization Self-Rotation

In practice, we use polarization self-rotation (PSR) to generate a squeezed state of light. It is known when an elliptically polarized light passes through a PSR medium, its polarization rotates at an angle ψ given by

$$\psi = g\epsilon(0)l \tag{5.11}$$

where g is a constant determined by the intensity and frequency of the incident light, $\epsilon(0)$ is the ellipticity, and l is the length of the medium. We use a strong linearly polarized light in $\hat{y}$ direction while it propagates along $\hat{z}$. Notice that we still have a vacuum field along polarized in $\hat{x}$ so we have a slightly elliptical polarized light with

$\epsilon(0) << 1$ and $\psi << 1$. For simplicity, we assume the ellipticity does not change much, that is, $\epsilon(0) = \epsilon(l) = \epsilon$. We further neglect the absorption of light by the medium.

Starting with the classic electromagnetism, a monochromatic light propagates in $\hat{z}$ direction has two components in $\hat{x}$, $\hat{y}$ such that $\hat{E}(z,t) = E_x(z,t)\hat{x} + E_y(z,t)\hat{y}$. We may also decompose the electric field into its positive and negative frequency components as $\hat{E}(z,t) = \hat{E}^+(z,t) + \hat{E}^-(z,t)$ where

$$\hat{E}^+(z,t) = \frac{\varepsilon_x(z)}{2} e^{i(kz-\omega t+\phi(z))}\hat{x} + \frac{\varepsilon_y(z)}{2} e^{i(kz-\omega t)}\hat{y}, \tag{5.12}$$

$$\hat{E}^-(z,t) = \frac{\varepsilon_x(z)}{2} e^{-i(kz-\omega t+\phi(z))}\hat{x} + \frac{\varepsilon_y(z)}{2} e^{-i(kz-\omega t)}\hat{y}, \tag{5.13}$$

ε_x, ε_y are real positive amplitudes of x, y polarized components, $k = \omega/c$ is the vacuum wave number, and $\phi(z)$ is a phase. In case of $\varepsilon_y(z) >> \varepsilon_x(z)$, the ellipicity of the light ϵ is approximately ([8])

$$\epsilon = \frac{\varepsilon_x(z)}{\varepsilon_y(z)} \sin(\phi(z)). \tag{5.14}$$

We only consider the $\hat{E}_x$ field as $\hat{E}_y$ would not be squeezed. For purpose of simplicity, we neglect the negative frequency component as well. After the medium, we have the positive $\hat{x}$ component as

$$E_x^+(l) = \varepsilon_x e^{i(kl-\omega t)} \left[e^{i\phi(0)} + gl \sin(\phi(0)) \right]. \tag{5.15}$$

Now, we switch to the QED description. As the squeezing is dependent on the phase χ, we write it as

$$\hat{E}_x(\chi, z) = \frac{\varepsilon_0}{2} \left[\hat{a}_x(z) e^{i\chi} + \hat{a}_x^+(z) e^{-i\chi} \right] \tag{5.16}$$

where we assumed the LO has the same frequency as the monochromatic light, χ is the time-independent phase difference between them at the output, and ε_0 is the characteristic amplitude of unsqueezed vacuum fluctuation [9]. We define the ellpiticity

operator

$$\hat{\epsilon} = \varepsilon_0 \frac{\hat{a}_x(z) - \hat{a}_x^\dagger(z)}{2i\varepsilon_y(z)} \tag{5.17}$$

such that $\langle \hat{\epsilon} \rangle = \epsilon$ for the coherent state. Rewriting Eq. 5.15 into operators, one may find the definition of the annihilation operator at the output as

$$\hat{a}_x(l) = \hat{a}_x(0) + \frac{igl}{2} \left[\hat{a}_x^+(0) - \hat{a}_x(0) \right]. \tag{5.18}$$

Eventually, using Eq. 5.16, we have the $\hat{x}$ polarized field after the PSR medium as

$$\hat{E}_x(\chi, l) = \frac{\varepsilon_0}{2} \hat{a}_x(0) \left(e^{i\chi} - igl \cos\chi \right) + \frac{\varepsilon_0}{2} \hat{a}_x^+(0) \left(e^{-i\chi} + igl \cos\chi \right) \tag{5.19}$$

with

$$(\Delta \hat{E}_x(\chi, l))^2 = \frac{\varepsilon_0^2}{4} \left(1 - 2gl \sin\chi \cos\chi + g^2 l^2 \cos^2\chi \right) \tag{5.20}$$

for an $\hat{x}$ polarized vacuum state $|0\rangle$ input [10]. Notice that the noise is phase dependent and we could get a smaller fluctuation than the vacuum field with a proper choice of χ.

Chapter 6

Squeezed Probe Beam

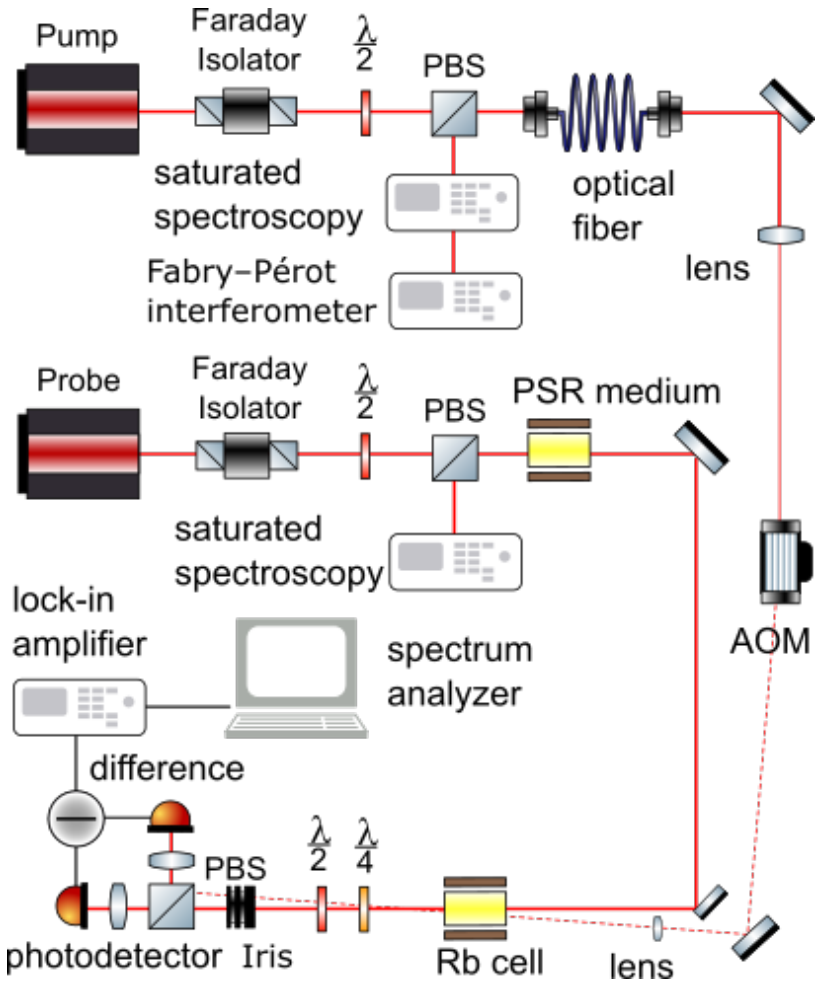

Figure 6.1: Neither laser is internally modulated. A dashed line represents an amplitude modulated laser while a solid line means unmodulated light.

In the two-beam configuration, we did a grid search on the laser power and optimized almost every parameter. Yet, we still cannot improve the sensitivity at side resonances lower than the nT level. After deploying all techniques, we think the sensitivity is now limited by the coherence time of the dark state, which is hard to improve without an anti-relaxation coating which increase the coherence time by reducing the collision between Rb atoms and the cell. However, the fabrication of the anti-relaxation coating remains as a "black magic" within each research group and there is no consent on it. Hence, we shift our focus from the state-of-art sensitivity to exploring the effect of a squeezed probe since this is still not a well-studied subject.

We use two individual laser sources for the probe and pump beam (Fig. 6.1). We directly use the laser from the last setup as the pump beam while removing the PBS before the AOM as the probe beam will come from another laser. Similar to the pump laser, we monitor the probe laser using saturated spectroscopy as well. We generate the squeezing in the probe beam using PSR discussed in the previous section. The PSR medium is another Rb cell and we use a half-waveplate and a PBS to control the probe power through the medium. The PBS also plays the role of a linear polarizer, so we take out the unnecessary polarizer before the Rb cell that induces Faraday rotation.

We only send one beam polarized in $\hat{y}$ through the medium and the squeezed light is generated from the vacuum field polarized in $\hat{x}$. Hence, after the PSR medium, the light consists of both a LO and the squeezed light which can be separated using a PBS later. After the Rb cell, we use a quarter waveplate to change the relative phase χ between the LO and the squeezed light. The beam is eventually evenly split by a PBS whose splitting ratio is controlled by a half waveplate and we detect the squeezing using balanced homodyne detection as discussed before.

6.1 Squeezing Strength

The strength of squeezing is determined by three factors: probe power, probe detuning, and PSR medium position, which can all be explained by Eq. 5.20. We find the optimal probe power is around 7 mW before the PSR medium and the optimal detuning is blue-detuned to the $2 \rightarrow 2$ transition. The medium position is adjusted according to the squeezing signal and remains fixed after that.

When the squeezed state of light experiences a loss, it is equivalent to passing it through a BS with another vacuum input and the output squeezing degrades because it is now a mix of squeezed light and coherent light. Hence, the squeezed state is extremely sensitive to lose which degrades significantly even with a small loss. Meanwhile, any misalignment also destroys the squeezed state since it is a loss.

As part of the light would be absorbed by the Rb cell, we first take out the Rb cell inducing Faraday rotation and check the squeezing. To measure the shot noise, we use a linear polarizer after the Rb cell to restore the coherent state. Then we adjust the quarter waveplate such that we have minimal noise for the squeezed light. The best squeezing we could get is about 1 dB (Fig. 6.2). Previously, this setup could generate squeezing up to 2 dB and we think our detection is still limited by alignment. Next, we put back the Rb cell and start the pump beam. We set the pump beam to intersect with the probe beam inside the Rb cell and the intersection angle is limited by our configuration. The absorption of the probe beam is about 10%. Surprisingly, we could observe a squeezing as large as 1.5 dB presumably because we accidentally have a better alignment with the Rb cell (Fig. 6.3).

As the absorption does not affect the squeezing much, we check whether the squeezing is strong enough to be observed using the lock-in amplifier. The lock-in amplifier has a few advantages over the spectrum analyzer. It is much cheaper and

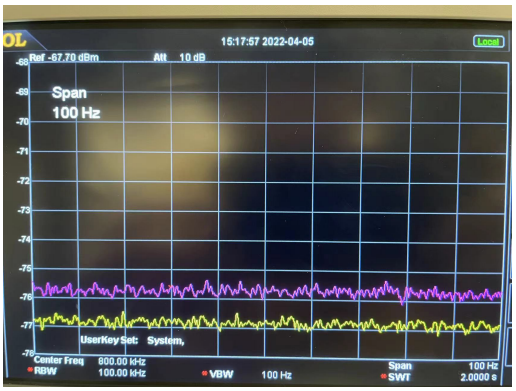

Figure 6.2: The purple line is the shot noise observed with a linear polarizer. The yellow line is the squeezed noise when the Rb cell is removed.

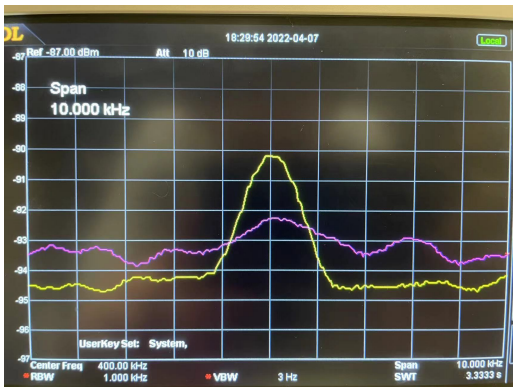

Figure 6.3: The purple line is the shot noise. The yellow line is the squeezed noise with a Faraday rotation signal in 400kHz.

it could measure a sweeping signal with a trigger. While the power and detuning of the probe beam are fixed to optimize the squeezing, we set the modulation frequency of the pump beam to 400 kHz. The pump detuning is at $2 \rightarrow 1$ transition and we use a weak pump beam with power around 150 μW to mitigate the effect of leakage of the pump beam into the detection. Since we are only interested in the noise level, we fix the magnetic field at side resonances. To further compare the effect of squeezing, we record the signal where we kill the squeezing before the Rb cell using a linear polarizer instead of after it. We find that the squeezing is still observable using the lock-in amplifier (Fig. 6.4)

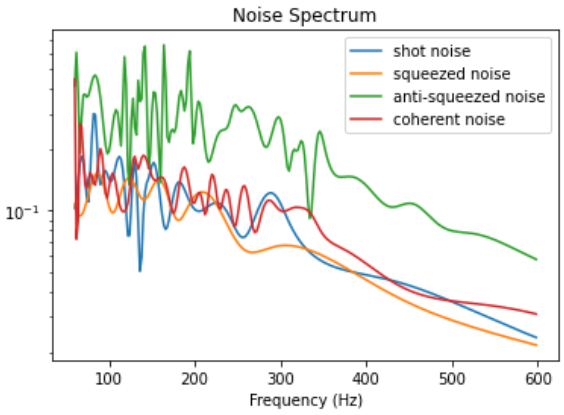

Figure 6.4: Coherent noise represents that we kill the squeezing before the Rb cell and the shot noise means that we kill the squeezing after the cell. Anti-squeezed noise is the most noisy quadrature of our signal.

6.2 Opposite Propagating Beams

In the current setup, when we block the probe beam, we can always observe a significant leakage signal if the pump beam is strong enough. We tried to use a lens to focus the pump beam. Yet, even the weakest Gaussian wing of the focus pump beam which is as low as 10 μW can still be detected by the SA. To completely solve this leakage problem, we redirect the pump beam so it propagates in the opposite direction of the probe beam (Fig. 6.5). We further use two additional irises before two lenses in front of the photodiodes to block large angle leakage that would be refracted into the detection by these lenses.

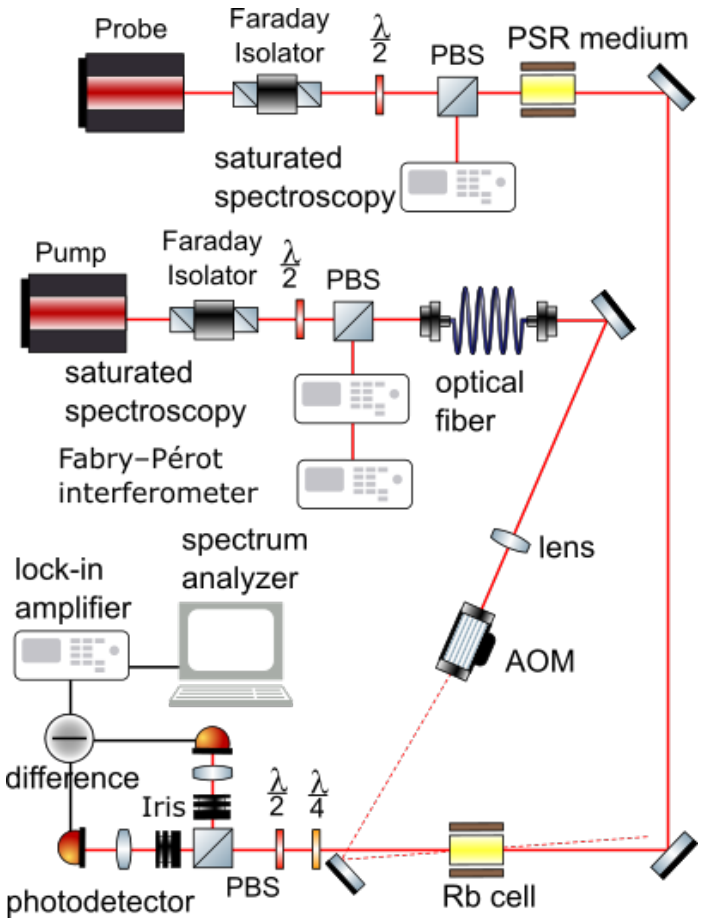

Figure 6.5: The pump beam propagates in an opposite direction with the probe beam and it blocked after the Rb cell.

After finished the setup for a pump beam propagating in the opposite direction with the probe beam. We confirmed that there is no leakage in the detection even for the strongest 2.5 mW pump beam. The noise level is also unchanged with respect to the change of the pump power indicating we only detect the probe beam. We again check that we can still distinguish coherent noise from squeezed noise using the lock-in amplifier (Fig. 6.6). Then we calculate the improvement of the SNR from the coherent light to the squeezed light. We find squeezed light has about 10-20% stronger response than coherent light (Fig. 6.7). Eventually, the SNR can be improved by a factor of 2 using the squeezed probe (Fig. 6.8).

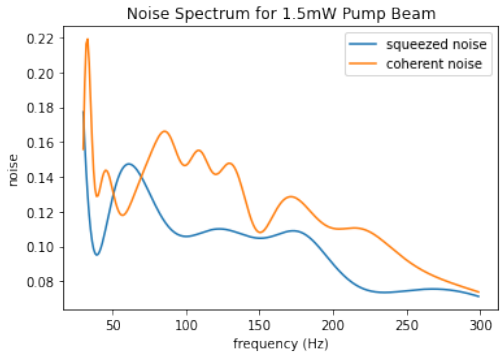

Figure 6.6: We can see a clear separation between the squeezed noise and the coherent noise.

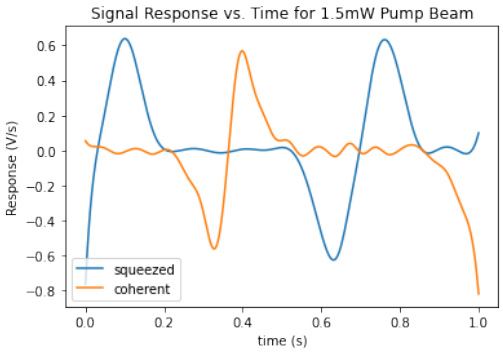

Figure 6.7: There are two periods of signal of the squeezed light and one period of the signal of the coherent light shown in this graph.

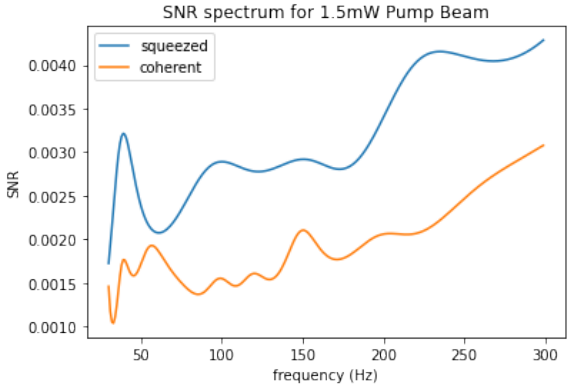

Figure 6.8: The squeezed light has both better response rate and lower noise level than the coherent light.

Chapter 7

Conclusion

Summary

In the first part of the experiment, we replace the amplitude modulated laser with a frequency-modulated laser to reduce amplitude fluctuation in our signals. However, because the cavity gain is dependent on the frequency, the FM also generates a spurious AM which results in a residue offset in our signal. We use a quarter-waveplate to balance the residual signal and a compensation coil to reduce the magnetic gradient. With this setup, we increase the sensitivity to 60 pT for the zero resonance.

Despite the sensitivity we achieved using a frequency-modulated laser, we separate our laser into a probe and pump beam to eliminate the residual signal. While we amplitude modulates the pump beam, we only detect the unmodulated probe beam, so we sidestep the residual signal. As the pump beam prepares Rb atoms into the dark state which interacts with the probe beam, we are still able to observe side resonances for the unmodulated probe beam. We conduct a grid search on the probe and pump power and optimize our signal according to the SNR. While we find the best sensitivity of side resonance is about the nT level, we think the sensitivity is limited by the coherence time of the dark state and is hard to improve without anti-relaxation coating. Yet, the two-beam configuration gives the additional spatial resolution of the magnetic field which cannot be achieved with a single beam.

Eventually, we generate a squeezed probe beam using polarization self-rotation. The setup could generate squeezing up to 2 dB. While about 10% of the probe beam is absorbed by the Rb cell, we still observe a significant squeezing of about 1.5 dB in our signal. We further compare the squeezed noise with the coherent noise and confirm a factor of 2 improvements in the SNR using the lock-in amplifier.

Future Work

This work shows that a sensitive magnetometer could be built based on NMOR. Without an anti-relaxation coating, its sensitivity could reach 60 pT at the zero resonance and nT level at the side resonance. Meanwhile, the intersection between the probe and pump beam allows us to measure a local magnetic field compared to the whole Rb cell. Limited by our configuration, we couldn't make a very large intersection angle. Yet, the preliminary data suggests that the intersection angle has minor effects on the sensitivity and a magnetometer focus on spatial mapping of the magnetic field is possible. On the other hand, squeezing could be implemented to the probe beam so we surpass the SNL. However, the method we generate the squeezing, PSR, put constraints on the probe power as well as its detuning. Since probe power certainly affects the sensitivity, one could separate the LO from the squeezed light and use a filter to reduce the probe power. This may reduce the stability of our system as re-mixing the LO and the squeezed state of light in the balanced homodyne detection is not an easy task to do.

References

[1] Volkmar Schultze et al. "An Optically Pumped Magnetometer Working in the Light-Shift Dispersed Mz Mode". In: *Sensors* 17.3 (Mar. 2017). Number: 3 Publisher: Multidisciplinary Digital Publishing Institute, p. 561. DOI: 10.3390/s17030561. URL: https://www.mdpi.com/1424-8220/17/3/561 (visited on 12/05/2021).

[2] Z. D. Grujić and A. Weis. "Atomic magnetic resonance induced by amplitude-, frequency-, or polarization-modulated light". In: *Physical Review A* 88.1 (July 12, 2013), p. 012508. ISSN: 1050-2947, 1094-1622. DOI: 10.1103/PhysRevA.88.012508. arXiv: 1305.6574. URL: http://arxiv.org/abs/1305.6574 (visited on 04/21/2021).

[3] David J. Griffiths. *Introduction to Quantum Mechanics*. Cambridge University Press, 2017. 481 pp. ISBN: 978-1-107-17986-8.

[4] Marlan O. Scully and M. Suhail Zubairy. *Quantum Optics*. Cambridge: Cambridge University Press, 1997. ISBN: 978-0-521-43595-6. DOI: 10.1017/CBO9780511813993. URL: https://www.cambridge.org/core/books/quantum-optics/08DC53888452CBC6CDC0F (visited on 04/22/2022).

[5] Vito Giovanni Lucivero et al. "Shot-noise-limited magnetometer with sub-picotesla sensitivity at room temperature". In: *Review of Scientific Instruments* 85.11 (Nov. 1, 2014). Publisher: American Institute of Physics, p. 113108. ISSN: 0034-6748. DOI: 10.1063/1.4901588. URL: https://aip.scitation.org/doi/10.1063/1.4901588 (visited on 11/19/2021).

[6] Ravn M. Jenkins, Eugeniy E. Mikhailov, and Irina Novikova. "Transit Ramsey EIT resonances in a Rb vacuum cell". In: *Journal of the Optical Society of America B* 36.4 (Apr. 1, 2019), p. 890. ISSN: 0740-3224, 1520-8540. DOI: 10.1364/JOSAB.36.000890. arXiv: 1807.10370. URL: http://arxiv.org/abs/1807.10370 (visited on 04/21/2022).

[7] Christopher Gerry and Peter Knight. *Introductory Quantum Optics*. 1st edition. Cambridge, UK ; New York: Cambridge University Press, Nov. 22, 2004. 332 pp. ISBN: 978-0-521-52735-4.

[8] Serge Huard. *Polarization of Light*. 1st edition. Chichester ; New York : Paris: Wiley, Feb. 25, 1997. 348 pp. ISBN: 978-0-471-96536-7.

[9] D. F. Walls. “Squeezed states of light”. In: *Nature* 306.5939 (Nov. 1983). Number: 5939 Publisher: Nature Publishing Group, pp. 141–146. ISSN: 1476-4687. DOI: 10.1038/306141a0. URL: https://www.nature.com/articles/306141a0 (visited on 04/08/2022).

[10] A. B. Matsko et al. “Vacuum squeezing in atomic media via self-rotation”. In: *Physical Review A* 66.4 (Oct. 30, 2002), p. 043815. ISSN: 1050-2947, 1094-1622. DOI: 10.1103/PhysRevA.66.043815. URL: https://link.aps.org/doi/10.1103/PhysRevA.66.043815 (visited on 04/08/2022).